

## DESIGN AND VALIDATION OF A SINGLE-JACK VARIABLE MACH NUMBER NOZZLE IN A CRYOGENIC TRANSONIC WIND TUNNEL

CHENGGUO YU

*Xi'an Research Institute of High Technology, Xi'an, Shaanxi Province, China, and  
China Aerodynamics Research and Development Center, Mianyang, Sichuan Province, China*

ZHILI ZHANG

*Xi'an Research Institute of High Technology, Xi'an, Shaanxi Province, China*

NING WANG, XUTAO NIE, QIANG PENG, ZHENHUA CHEN

*China Aerodynamics Research and Development Center, Mianyang, Sichuan Province, China  
Corresponding author Zhenhua Chen, e-mail: [chenzhenhua@cardc.cn](mailto:chenzhenhua@cardc.cn)*

The wind tunnel with variable Mach numbers controlled by a single jack is highly desired in the aerospace, automobile and building industry due to its superior controllability and working range. Decreasing the temperature of a test gas is an efficient and economical approach to achieving higher Reynolds numbers that accommodate all working statuses of test subjects, which however, brings new challenges to the wind tunnel design nowadays. This paper proposes a new design concept of a single-jack variable Mach number nozzle based on its particular cryogenic characteristics, as the nozzle is the core structure to achieve variable Mach numbers. The contours of the nozzle under different Reynolds numbers and Mach numbers are modeled and solved by an incomplete elliptic integral, followed by modification with cryogenic characteristics. A 0.3-m cryogenic wind tunnel is utilized as a validation platform for the nozzle design, resulting in designed contours being in line with the measured contours. Moreover, the root means square (RMS) deviations of Mach number 1.3 at the core position are controlled within 0.011 in low and high temperatures, which surpasses the other existing wind tunnels.

*Keywords:* cryogenic, flow uniformity, single-jack nozzle, transonic wind tunnel, variable Mach number

### 1. Introduction

The wind tunnel is the essential equipment to carry out model testing, ranging from advanced aircraft, naval ships to high buildings. In the aerospace engineering, data from wind tunnel experiments dominate the aerodynamics design of the aircraft. With development of advanced high-speed planes and aerospace craft, the flight Reynolds number and its coupling effects have been considered in the design process (Zhang and Niu, 2015). Therefore, the cryogenic wind tunnel providing the flow of real-flight Reynolds numbers at certain temperatures has been highly desired and rapidly growing in recent years (Niu and Yu, 2021).

Nowadays, a few countries have the ability to build a cryogenic high-Reynolds number wind tunnel. Table 1 shows specification of five typical cryogenic transonic wind tunnels, including the two largest transonic high-Reynolds number cryogenic wind tunnels in the world and the 0.3-m cryogenic wind tunnel (0.3CW) presented in this paper. At a given Mach number, several approaches are used to increase the Reynolds number including, but not limited to using a heavy testing gas rather than the air, increasing both the size of the wind tunnel and the test model, increasing the operating pressure of the wind tunnel, and reducing the test temperature. It is unaffordable, however, to achieve a high Reynolds number by merely increasing the size of wind

tunnels (Liao *et al.*, 2014). The use of a heavy gas or higher pressure can set limitations size of the wind tunnel. Decreasing the temperature of the test gas is a promising way to increase the Reynolds number. Thus, the cryogenic wind tunnel comes forward and enjoys the advantages of decreasing the dynamic pressure and drive power, reducing construction cost, decreasing peak power and energy consumption, and having unique operation capability. Therefore, cryogenic wind tunnels with high Reynolds numbers are developed extensively.

**Table 1.** Specification of typical cryogenic wind tunnels

Wind tunnel	Temperature [K]	Mach number	Test section size [m]	Pressure [100 kPa]
NTF	111-327	0.1-1.2	$2.5 \times 2.5$	1-9
ETW	110-313	0.15-1.3	$2.4 \times 2.0$	1.25-4.5
0.3TCT	80-320	0.2-0.85	$0.33 \times 0.33$	1.2-6.0
PETW	90-313	0.35-1.00	$0.23 \times 0.27$	1.25-4.50
		1.2		
		1.35		
0.3CW	110-323	0.15-1.30	$0.325 \times 0.275$	0.2-4.5

The 0.3-m transonic cryogenic tunnel (0.3TCT) in the NASA Langley Research Center is the first cryogenic transonic wind tunnel in the world. Its maximum Mach number can reach 0.85 only (Reese *et al.*, 2019), thus making it lagging behind. The Pilot European Transonic Wind (PETW) tunnel is the pilot wind tunnel of the European Transonic Wind (ETW) tunnel, which employs a replaceable throat block to control the Mach number by using three sets of nozzle blocks, including subsonic flow and Mach numbers 1.2 and 1.35, respectively (Hensch *et al.*, 2019). However, the operation of changing the throat is a time-consuming process. As the first large-scale production-type cryogenic transonic wind tunnel, the National Transonic Facility (NTF) in America adopts the air extraction method in the chamber and achieves the maximum Mach number 1.2 (Rivers *et al.*, 2019). The ETW was built in 1993 by four European countries (Britain, France, Netherlands, and Germany) (Hartzuiker, 1984). While designing this tunnel, the designer considered a movable block and a single-jack nozzle to build the first in situ variable nozzles. The position of the movable block sets the Mach number in the test section, and the actuator on the free part of the flexible plate determines its longitudinal distribution (Hartzuiker, 1986). A variable Mach number nozzle can improve the flow field quality in a transonic wind tunnel, reduce the compressor power requirement and enhance test efficiency (Green and Quest, 2011).

Over the past few decades, the pursuit of wind tunnel design has led to some great achievements in studying the variable Mach number nozzle. In 1929, Prandtl and Busemann worked out a notable graphical method, which has been used since then. After that, Puckett modified the graphical method to a semi-graphical one. Foelsch proposed an analytical design method based on the fundamental ideas used by Prandtl and Busemann in solving the problem graphically. Cresci (1958) and Sivells (1978) obtained a continuous curvature curve by setting a partial cancellation region, which significantly improved the coincidence accuracy between the aerodynamic and elastic contour of the flexible nozzle.

Rosen (1955) proposed a single-jack flexible nozzle using a flexible plate with linear thickness distribution to obtain the design contour through bending deformation. Subsequently, many researchers adopted Rosen's concept in their works (Chen *et al.*, 2016; Lv *et al.*, 2018). However, no published study has reported on the nozzle design method of variable Mach numbers considering the fluid-solid-thermal coupling problem in a cryogenic environment.

Compared with room-temperature wind tunnels, the boundary layer is thinner in a cryogenic wind tunnel (Kittel, 2012). As a result, the coincidence of the elastic line and the aerodynamic theoretical line influences the flow quality. The thermal effects on the Reynolds number and

pressure variations have not been considered in previous studies. In addition, deviations between the flexible plate elastic line using the small-deflection approximation method and the actual line increase under a large deformation. The elliptic integral method offers a simple approach to solve this classic large-deflection beam problem. Bisschopp and Drucker (1945) studied the elliptic integral solution of a large-deflection beam under a vertical load and gave a relative deviation between the elliptic integral solution and the approximate solution of the small-deflection beam. Howell and Leonard (1997) studied elliptic product decomposition of a cantilever beam under combined action of a force and bending moment. Zhang and Chen (2013) proposed a complete elliptic integral solution method for a complex bending problem of plane beams with multiple inflection points, thus expanding the solution ability of the elliptic integral method. Xu *et al.* (2021) studied the accurate solution of large deflection of composite elastic beams based on the elliptic integral. Inspired by the previous studies, this method in the design of the cryogenic wind tunnel is explored in this paper. The aims of this study were as follows:

- (1) design the aerodynamic contour of a variable Mach number nozzle taking into account high and low Reynolds numbers;
- (2) analyze deviation between the elastic contour and aerodynamic contour under a large-deflection deformation and give the middle Mach number contour;
- (3) verify the design theory using an experimental facility.

The design and validation of the cryogenic variable Mach number nozzle were explored to provide theoretical tools for design and construction of large cryogenic transonic wind tunnels.

In the first part of this study, a single-jack variable Mach number nozzle design method based on large-deflection deformation theory is proposed for a cryogenic transonic wind tunnel. In the second part, the variable Mach number nozzle for 0.3-m cryogenic transonic wind tunnel (0.3CW) is designed and calibrated. The flow field results in a wide temperature range are discussed in the third part, which validated the concepts of our design. The RMS deviations of Mach numbers at the core position are controlled within 0.011 in low and high temperatures, which surpasses the other existing wind tunnels.

## 2. Design methodology

### 2.1. Aerodynamic contour design

The viscosity of the airflow is usually ignored in the design of the contour, a nozzle curve is obtained, and then the boundary layer is corrected by considering the viscosity of the air flow.

Figure 1 shows the contour of a nozzle, proposed by Foelsch, including a throat area, an initial expansion section, and a full-wave cancellation section.

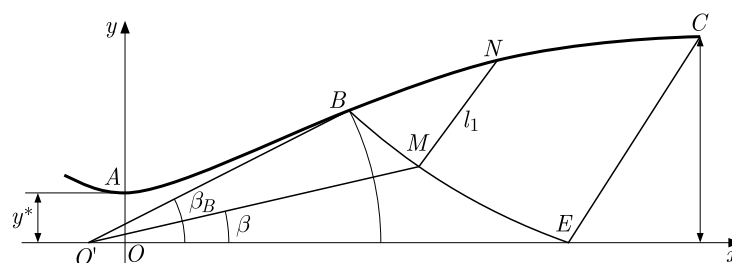


Fig. 1. Design features of a Foelsch contour

It is assumed that the radial flow from point  $O'$  is converted into a parallel stream with uniform velocity. The arc size of the throat area is determined using the maximum Mach number and outlet height. Then, the curve from point  $B$  to  $C$  is calculated using the method of characteristics.

In the initial expansion section, a polynomial curve in Eq. (2.1) is used to meet the radial flow assumption at the inflection point  $B$

$$y = y^* + \frac{\tan \beta_B}{x_B} x^2 \left( \frac{1-x}{3x_B} \right) \quad (2.1)$$

The  $\beta_B$  was suggested as

$$\beta_B = \frac{1}{2} \nu_1 \left( \frac{y^*}{h} \right)^{\frac{2}{9}} \quad (2.2)$$

where  $\nu_1$  is the Prandtl-Meyer angle,  $y^*$  represents the half-height of the throat, and  $h$  denotes the half-height of the outlet. In the full-wave cancellation section, the coordinates of point  $N$  at the nozzle wall are

$$\begin{aligned} x_N &= x_B + r \cos \beta - r_B \cos \beta_B + l_1 \cos(\beta + \mu) \\ y_N &= r \sin \beta + l_1 \sin(\beta + \mu) \end{aligned} \quad (2.3)$$

where  $\beta$  is the angle  $MO'E$ ,  $l_1$  represents length of  $MN$ ,  $r$  represents length of  $O'M$ , and  $\mu$  denotes the angle between  $O'M$  and the Mach line.

According to the method proposed by Foelsch, the curvature is not a straight line, which requires the linear-thickness plate to match the flexible plate contour. In this study, however, the curvature is approximately a straight line at a low supersonic Mach number. An equal-thickness flexible plate is used for the full-wave cancellation region to reduce the difficulty of manufacturing.

## 2.2. Boundary layer correction

Because of the viscous effect, the real flow was quite different from the inviscid flow. The air viscosity led to a contoured-wall boundary layer, which changed the nozzle cross-section distribution and the Mach number distribution (Fig. 2). The internal nozzle wave interfered with the boundary layer on the nozzle contour wall, which affected the flow in the boundary layer and changed the development and reflection of the wave. Therefore, the reflection of the expansion wave could not be eliminated in the design of the non-viscous flow.

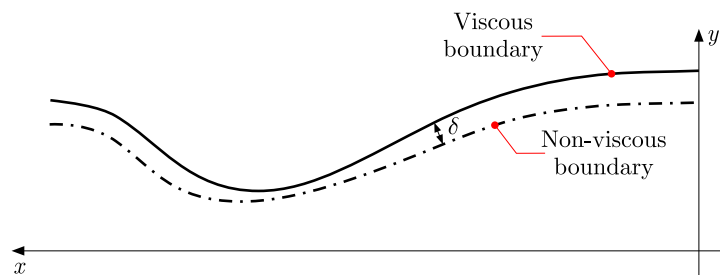


Fig. 2. Non-viscous and viscous boundaries

To meet the flow velocity and uniformity requirement in the test section, it was necessary to consider a correction in the boundary layer increment to obtain physical coordinates of the nozzle contour.

According to the boundary layer correction theory and experimental results, the boundary layer thickness in the supersonic contour was found to increase approximately linearly along with the wind tunnel axis. Assuming that the thickness of the boundary layer at the throat was zero, Davis *et al.* (1987) pointed out that when the Mach number was less than 2.5, the average

thickness growth rate of the boundary layer in the supersonic section was as in the following equation

$$\frac{d\delta}{dx} = \frac{0.29}{\sqrt[5]{Re_L}} \quad (2.4)$$

where  $Re_L$  is the Reynolds number calculated from the parameters of the test section and length of the supersonic section of the nozzle. The equation showed that the growth rate of the boundary layer decreased with an increase in the Reynolds number.

### 2.3. Elastic deformation of the flexible plate

The subsonic contour was generated by rotating the throat block such that the flexible plate was straight and aligned with the exit angle. The single-jack nozzle mechanism under subsonic conditions is shown in Fig. 3. The length of the flexible plate was equal to the curve length from the inflection point to the outlet point, while the thickness of the flexible plate was decided by the allowable stress and aerodynamic pressure.

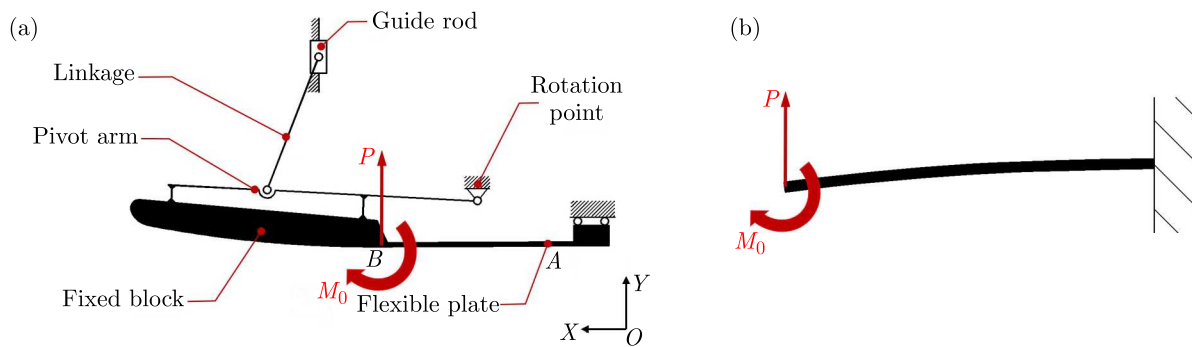


Fig. 3. Single-jack nozzle in the cryogenic wind tunnel: (a) mechanism diagram, (b) mechanical model

As an elastic component, the maximum deflection of a flexible plate is often far beyond the assumption of small deflection. According to Euler-Bernoulli beam theory, the relationship between curvature and bending moment satisfies the following equation

$$\frac{d\theta}{ds} = \frac{1}{\rho} = -\frac{M}{EI} \quad (2.5)$$

where  $\rho$  is the plate bending radius,  $M$  denotes the moment,  $E$  denotes the modulus of elasticity, and  $I$  represents the cross-sectional moment of inertia.

According to the definition of curvature, Eq. (2.5) could be equivalently written as

$$\frac{1}{\rho} = \frac{y''}{\sqrt{(1+y'^2)^3}} = -\frac{M(x)}{EI} \quad (2.6)$$

For a small-deflection condition  $y' \ll 1$ , omitting this term, the following equation is obtained

$$y'' = -\frac{M(x)}{EI} \quad (2.7)$$

The solution to this equation is quite simple, but the calculation accuracy is not high. The elliptic integral solution could provide an exact solution.

At any point, the moment in Fig. 3 is

$$M(x) = M_0 + P(x_B - x) \quad (2.8)$$

where  $M_0$  is the moment,  $P$  denotes the concentrated force, and  $x_B$  is the horizontal coordinate. All the aforementioned characteristics are at the upstream end.

Based on Equations (2.5) and (2.8)

$$\frac{d\theta}{ds} = -\frac{M_0 + P(x_B - x)}{EI} \quad (2.9)$$

Differentiating Eq. (2.9) with aspect to  $s$  once

$$\frac{d}{ds} \left( \frac{d\theta}{ds} \right) = \frac{P}{EI} \frac{dx}{ds} \quad (2.10)$$

in the micro section, the relationship between  $dx$ ,  $dy$ , and  $ds$  is

$$dy = \sin \theta ds \quad dx = \cos \theta ds \quad (2.11)$$

Now define  $\alpha = \sqrt{(P/EI)}$ ; then an equivalent expression of Eq. (2.10) becomes

$$\frac{d}{ds} \left( \frac{d\theta}{ds} \right) = \alpha^2 \cos \theta \quad (2.12)$$

Multiplying Eq. (2.12) by  $d\theta$

$$\frac{d\theta}{ds} d \left( \frac{d\theta}{ds} \right) = \alpha^2 \cos \theta d\theta \quad (2.13)$$

and integrating equation (2.13)

$$\int \frac{d\theta}{ds} d \left( \frac{d\theta}{ds} \right) = \alpha^2 \int \cos \theta d\theta + C \quad \frac{1}{2} \left( \frac{d\theta}{ds} \right)^2 = \alpha^2 \sin \theta + C \quad (2.14)$$

the boundary conditions at the upstream of the flexible plate is

$$M(x_B) = -M_0 \quad \theta = \theta_B \quad \frac{d\theta}{ds} = \frac{M_0}{EI} \quad (2.15)$$

Then, the constant  $C$  can be derived

$$C = \frac{1}{2} \left( \frac{M_0}{EI} \right)^2 - \alpha^2 \sin \theta_B \quad (2.16)$$

The relationship between  $ds$  and  $d\theta$  can be written as

$$\sqrt{2} ds = \frac{1}{\alpha \sqrt{\sin \theta - \sin \theta_B + k}} d\theta \quad (2.17)$$

in which,  $k = M_0^2 / (2PEI)$ . Integrating Eq. (2.17), where the left-hand side is from 0 to  $l$  and the right-hand side is from 0 to  $\theta_B$ , the following equation is obtained

$$\sqrt{2} l = \int_0^{\theta_B} \frac{1}{\alpha \sqrt{\sin \theta - \sin \theta_B + k}} d\theta \quad (2.18)$$

Equation (2.18) shows the relationship between the plate arc length and the rotation angle. Inserting Eq. (2.11) into Equation (2.17) and then integrating like Eq. (2.18), are obtains

$$\sqrt{2} y_1 = \int_0^{\theta_B} \frac{\sin \theta}{\alpha \sqrt{\sin \theta - \sin \theta_B + k}} d\theta \quad (2.19)$$

Equations (2.18) and (2.19) can be expressed as elliptic integrals

$$l = \frac{\sqrt{2}}{\alpha\lambda} f \quad y_1 = \frac{\sqrt{2}}{\alpha\lambda} (f + \lambda^2 e) \quad (2.20)$$

where

$$\lambda = \sqrt{\sin\theta_B - k - 1} \quad f = F(\gamma_1, t) - F(\gamma_2, t) \quad e = E(\gamma_1, t) - E(\gamma_2, t)$$

in which  $F$  is the first kind of an incomplete elliptic integral, and  $E$  is the second kind of an incomplete elliptic integral, and where

$$\gamma_1 = \sqrt{\frac{k}{-\sin\theta_B + k - 1}} \quad \gamma_2 = \sqrt{\frac{\sin\theta_B - k}{\sin\theta_B - k + 1}} \quad t = \sqrt{\frac{\sin\theta_B - k + 1}{\sin\theta_B - k - 1}}$$

After calculating the coordinates and deflection angle of the neutral curve of the flexible plate, the coordinates and deflection angle of the inner flow contour could be solved by the curve offset, which is expressed as

$$\begin{aligned} x &= \frac{\sqrt{2}}{\alpha} \left( \sqrt{k - \sin\theta_B} + \sqrt{\sin\theta_x + k - \sin\theta_B} \right) - x' - \frac{h}{2} \sin\theta_x \\ y &= \frac{\sqrt{2}}{\alpha} \frac{1}{\lambda} [f' + (k - \sin\theta_B + 1)e'] + \frac{h}{2} \cos\theta_x \end{aligned} \quad (2.21)$$

where

$$f' = F(\gamma'_1, t) - F(\gamma_2, t) \quad e' = E(\gamma'_1, t) - E(\gamma_2, t) \quad \gamma_1 = \sqrt{\frac{\sin\theta_x + k - \sin\theta_B}{k - \sin\theta_B - 1}}$$

### 3. Design case and experiment

Based on the design method presented in Section 2, a variable Mach number nozzle for the 0.3-m cryogenic wind tunnel (Fig. 4) was built in China Aerodynamic Development and Research Center. The wind tunnel was a cryogenic, continuous transonic wind tunnel, which could operate at the room-temperature air and low-temperature nitrogen (Lai *et al.*, 2020). For the room-temperature air, a high-efficiency heat exchanger (water cooling) in front of the third corner was used to absorb and balance the heat released by the compressor. When the low-temperature nitrogen was applied as the operating medium, the liquid nitrogen was injected into the tunnel through the liquid nitrogen injection section to realize the low-temperature operation.

The total pressure and temperature ranges in the settling chamber were  $(0.2\text{--}4.5) \cdot 10^5$  Pa and 110 K–323 K, respectively. The cross-sectional size of the test section was 325 mm × 275 mm. The characteristic Reynolds number was  $7 \cdot 10^6$ . The nozzle could produce three types of contours, including subsonic, Mach number 1.15 and Mach number 1.3.

The throat radius of 1528 mm was chosen for the throat arc, which was much larger than that proposed by Rosen (1955). The final value was also adjusted to allow a valid solution for the subsonic contour compatible with the overall length of the nozzle. The contours of the initial expansion section and the full-wave cancellation section were generated and modified using the boundary layer correction method mentioned earlier.

Figure 5a shows the aerodynamic contour under the maximum and minimum Reynolds numbers corresponding to flow Mach number 1.3. The highest Reynolds number was  $7.325 \cdot 10^6$ , corresponding to a total temperature of 110 K and a total pressure of 0.343 MPa. The lowest Reynolds number was  $8.82 \cdot 10^5$ , corresponding to a total temperature of 323 K and a total

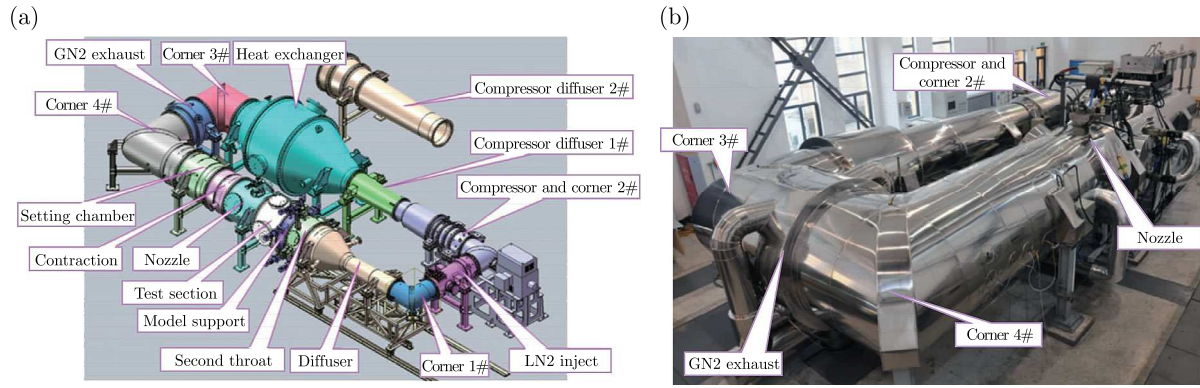


Fig. 4. 0.3-m cryogenic wind tunnel

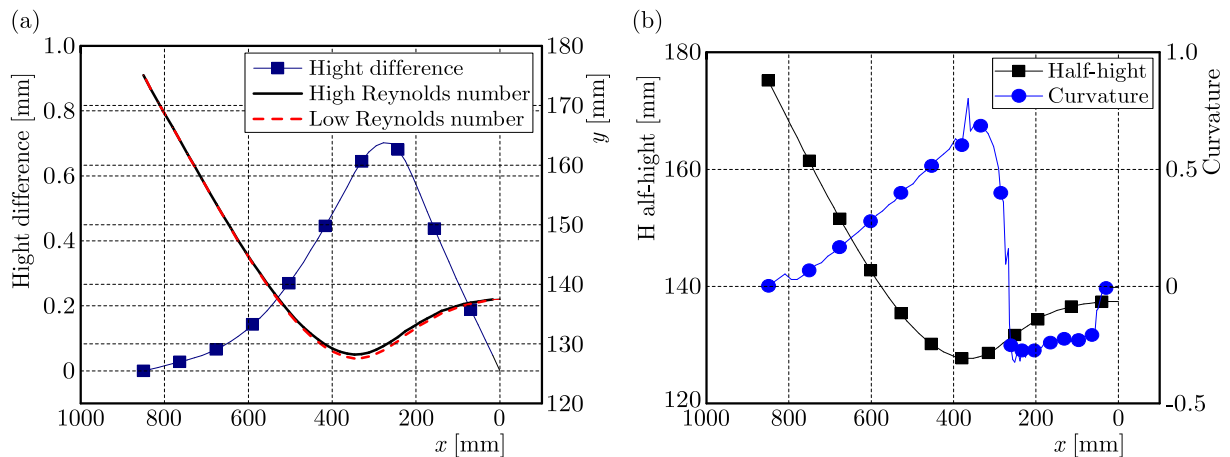


Fig. 5. (a) High- and low-Reynolds number contours. (b) Final aerodynamic contour and curvature

pressure of 0.02 MPa. The maximum deviation of the two contours was about 0.7 mm, and the exit angle was  $0.199^\circ$  and  $0.364^\circ$ , respectively.

Taking into account the high and low Reynolds numbers, a middle angle of  $0.28^\circ$  was chosen as the exit angle of the final aerodynamic contour. The nozzle contour was recalculated according to the design method. Figure 5b shows the final aerodynamic contour and its curvature. It demonstrates that the curvature of the flexible plate is approximately a straight line, and this part can be shaped by deforming the flexible plate of equal thickness.

The fixed block that defined the nozzle throat rotated about a node point located at the intersection of the tangent line from the inflection point and the tangent line from the nozzle exit. We obtained the subsonic contour by rotating the fixed block to the existing angle. The coordinates for Mach numbers 1.15 and 1.3 were computed from Eqs. (2.17) and (2.18).

The three contours are shown in Fig. 6, and the key geometric parameters are shown in Table 2.

**Table 2.** Key dimensional parameters of the nozzle

Flexible plate length	Flexible plate thickness	Outlet angle	Throat radius
217.1 mm	5 mm	$0.28^\circ$	1528 mm

Figure 7a shows a three-dimensional view to the single-jack semi-flexible wall nozzle, including a settling chamber, motor, screw jack, transmission bar, linkage, pivot arm, flexible plate and two side walls. The photo of the single-jack nozzle is shown in Fig. 7b, in which the fixed block and the flexible plate are manufactured as an integral component using N50 stainless

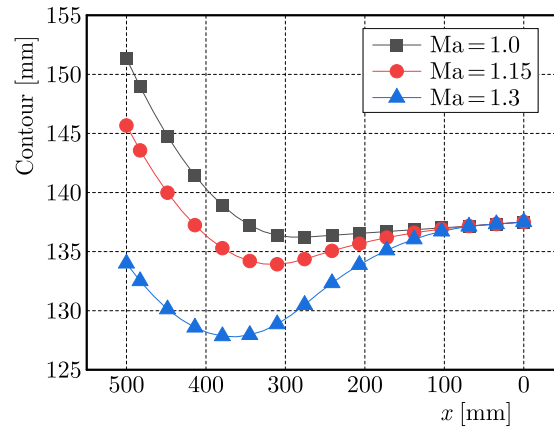


Fig. 6. Design contour of the single-jack nozzle

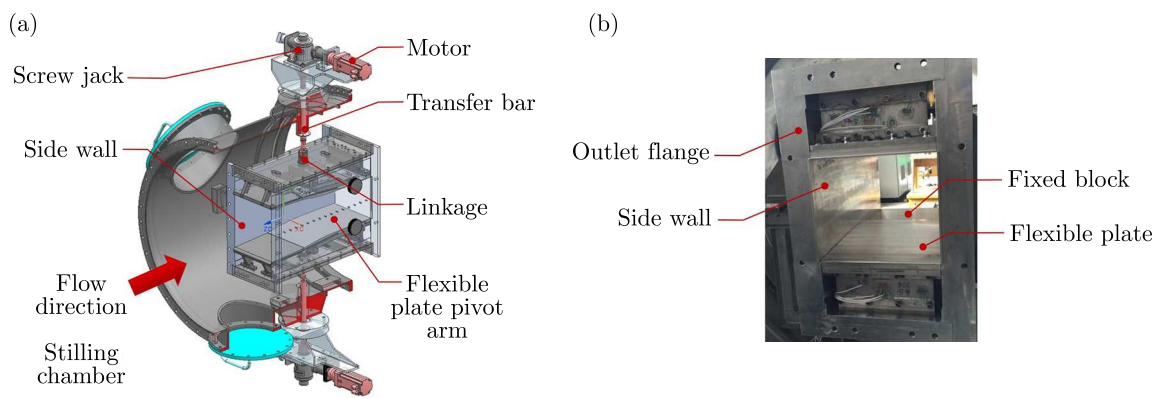


Fig. 7. (a) Model of the single-jack nozzle, (b) photograph of the single-jack nozzle

steel. The thickness of the flexible plate and the throat fixed block are 5 mm and about 30 mm, respectively.

A laser tracker was used to measure the inner flow contour coordinates of the nozzle when the reference point was selected on the mounting frame, and a space coordinate system was established with the nozzle outlet position as the coordinate origin. The  $x$ -axis was along the axis of the wind tunnel against the flow direction, and the  $y$ -axis was perpendicular to the axis of the wind tunnel and pointed to the outside of the tunnel.

In subsonic and transonic wind tunnels, the Mach number distribution on the centerline represent the distribution of the whole test section. During calibration, the axial probe pipe is installed in the center line of the test section to measure the static pressure distribution, and the Mach number is calculated with the total pressure. As shown in Fig. 8, the tail of the axial probe pipe is fixed to the model support structure of the test section. The head is fixed in the hole with four wires, and the steel wires are tensioned to prevent shaking.

The Mach number  $Ma$  at each measuring point is obtained using the following equation

$$Ma = \sqrt{5 \left[ \left( \frac{p_0}{p} \right)^{2/7} - 1 \right]} \quad (3.1)$$

where  $p_0$  is the total pressure of the settling chamber, and  $p$  is the static pressure measured by the axial probe pipe.

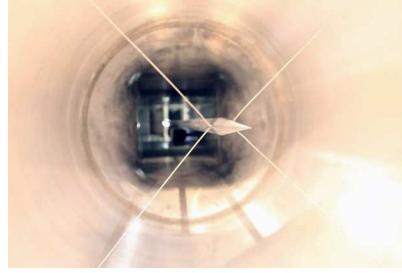


Fig. 8. Axial probe pipe in the wind tunnel

#### 4. Results and discussion

Figure 9 shows high accuracy of our design model in predicting aerodynamic contours. The maximum deviations were within 0.1 mm and 0.05 mm for Mach numbers 1.3 and 1.15, respectively. With an increase in flexible plate deformation, the deviation at the nozzle exit position increased, which was induced by the rigid body assumption on the nozzle exit. When the flexible plate was bent, the fixed point of the exit also had a certain elastic deformation, leading to a larger contour deviation.

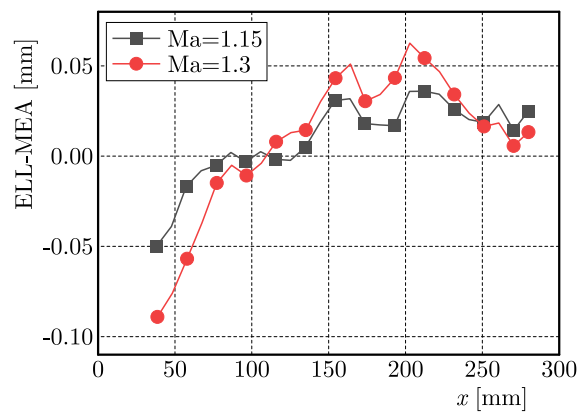


Fig. 9. Deviations between design and measurement results

A series of flow field calibration tests were carried out, and the Mach number distribution along the nozzle section and the core area of the test section was obtained.

Figure 10 shows the Mach number distribution along the nozzle axis at different temperatures. Figures 10a-10f represent Mach numbers of 0.3, 0.6, 0.9, 1.0, 1.15 and 1.3, respectively. At the upstream of the nozzle throat, the airflow accelerated dramatically for all six Mach numbers. But at the downstream of the throat, different regularity formed at different speeds. Under three low-speed conditions, the airflow speed substantially changed. While for the three high-speed conditions, the airflow speed downstream the throat slightly increased. In addition, it occurred that the Mach number deviation was little under different temperatures, while the Mach numbers along the nozzle axis increased gradually.

Figure 11a shows the Mach number deviations in the test section at 280 K, 200 K, and 110 K. The horizontal coordinate represents the average Mach number, and the vertical coordinate represents the deviation between the calibration Mach number and the setting Mach number. The results suggested that the Mach number in the test section slightly declined as the temperature decreased. Under the three temperature conditions, the Mach number decreased in the subsonic range down to 0.002, while it reached 0.004-0.006 at Mach numbers 1.0, 1.15 and 1.3.

For the subsonic condition, the airflow velocity mainly depended on the cross-sectional area ratio of the contraction entrance to the test section entrance. When the air temperature reduced,

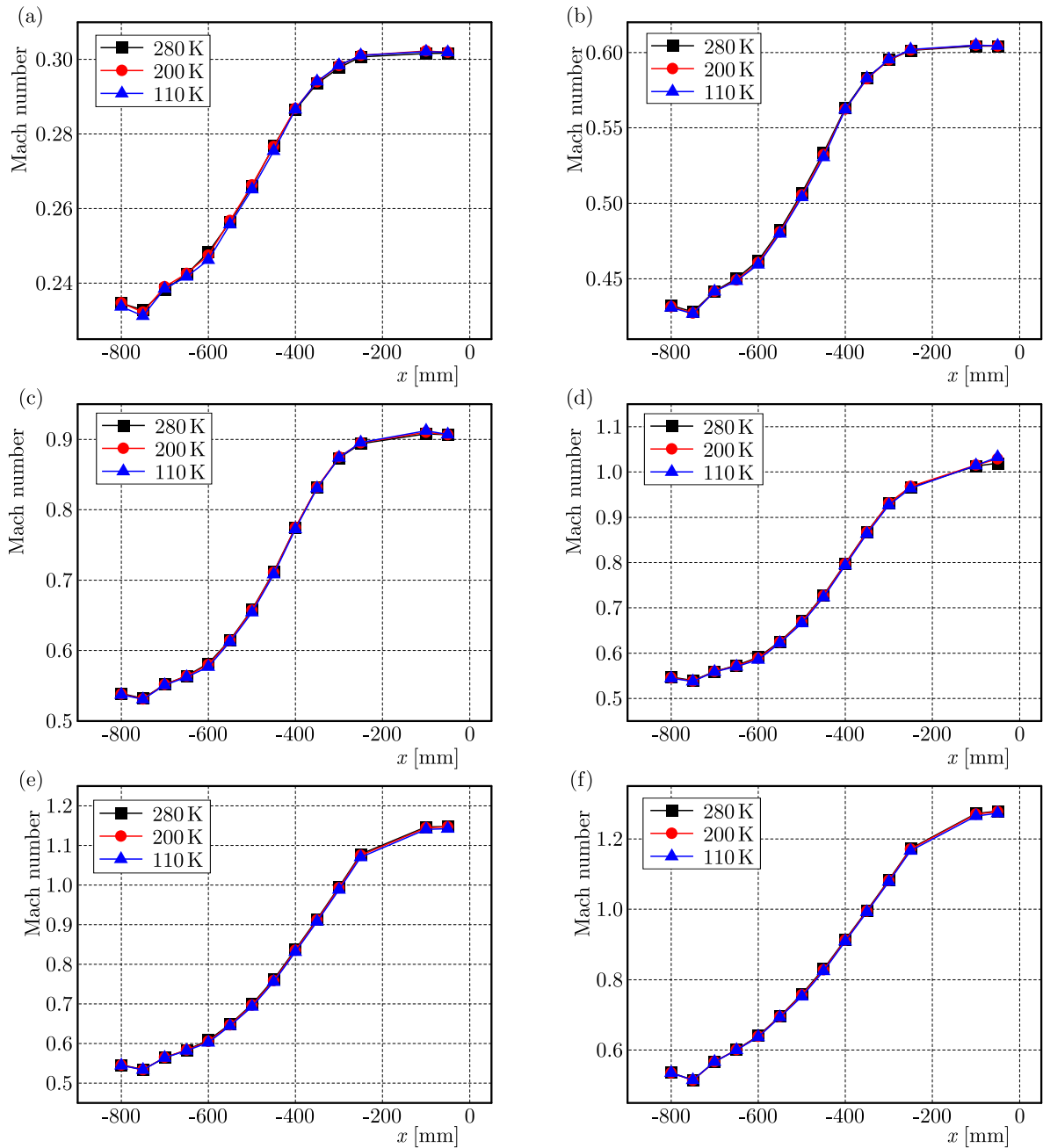


Fig. 10. Mach number distribution at different temperatures

the boundary layer became thin. The cross-sectional area of the test section entrance became relatively larger, resulting in a slight decrease in the airflow velocity.

In the supersonic state, the test section entrance cross-sectional area also increased as the temperature decreased. However, the airflow velocity mainly depended on the area ratio of the nozzle outlet to the throat due to the shut-off effect of the throat. The driving mechanism of the throat block was located outside the chamber leading to a large temperature difference between the inner channel airflow and the chamber. As a result, the size of the connecting linkage was relatively larger than the size of the inner flow channel component. Also, the area ratio of the outlet of the nozzle to the throat became larger resulting in a decrease in the airflow Mach number.

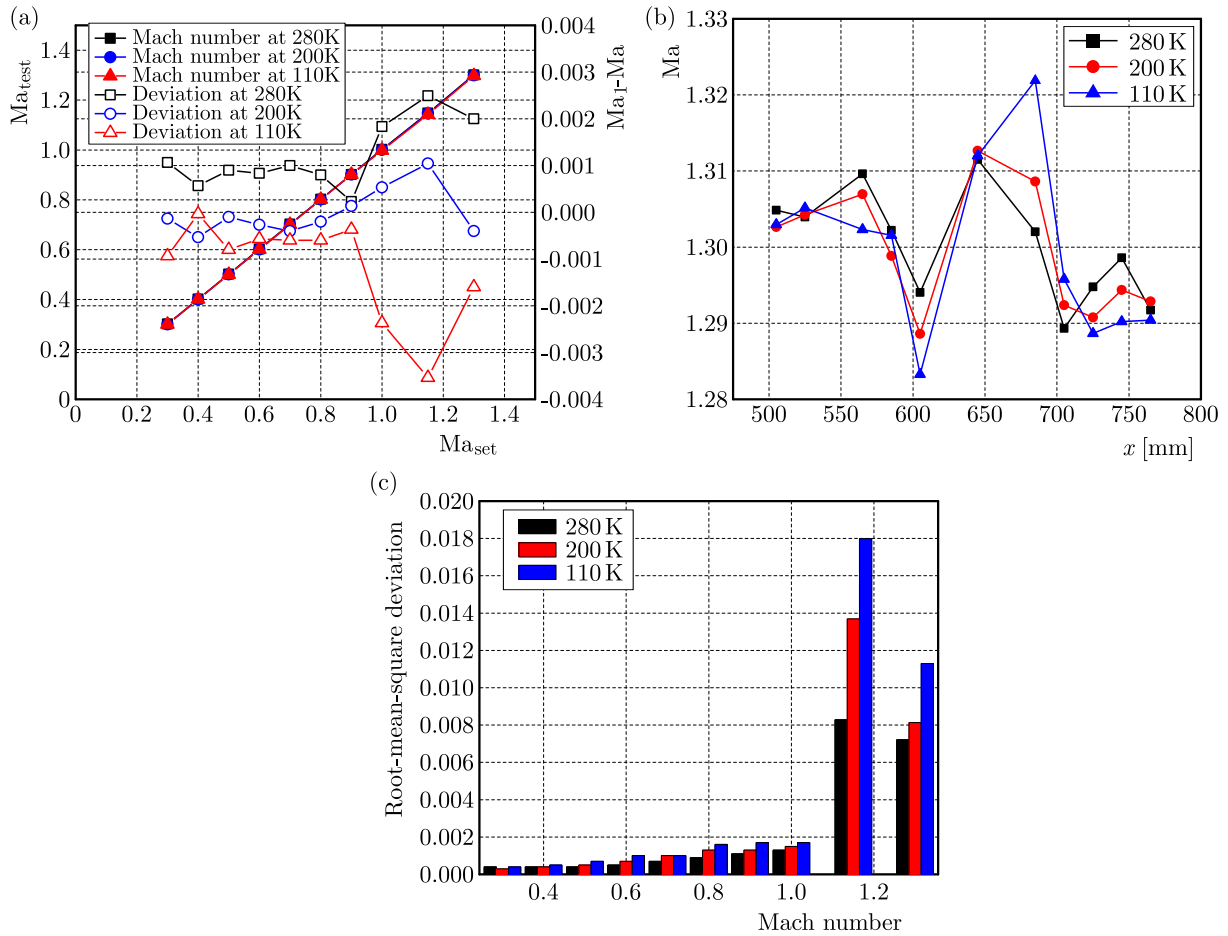


Fig. 11. (a) Mach number and deviations at different temperatures, (b) Mach number distribution in the core area, (c) Mach number root-mean-square deviation

Figure 11b shows the Mach number distribution in the core area of the test section calculated from the static pressure point data of the shaft probe tube under the working condition of Mach number 1.3. Figure 11c shows the core-flow Mach number root-mean-square (RMS) deviation with the air velocity under different temperature conditions. It suggests that under subsonic conditions, the Mach number RMS deviation was not greater than 0.002. The deviation in Mach number 1.3 condition was about 0.007 at 280 K. The RMS deviation increased to no more than 0.011 with a decrease in temperature. Compared with Mach number 1.3 and subsonic conditions, the flow field quality of Mach number 1.15 was worse, and the maximum RMS deviation was 0.018. The quality of the flow field deteriorated as the temperature decreased. The main reason was that the wind tunnel was small in size and the drive mechanism was placed outside the tunnel. A large temperature gradient existed in the structure at low temperatures, leading to uncoordinated structural deformation, especially for a low supersonic speed. The RMS deviation of the airflow had a greater impact.

In the room-temperature range ( $> 200$  K), the overall quality of the flow field in our cryogenic wind tunnel was superior to the index from China Military Standards for room-temperature wind tunnels. According to (Green and Quest, 2011), the Mach number uniformity in ETW shows a maximum deviation of 0.001 in subsonic conditions and 0.008 in supersonic conditions. In the subsonic and transonic stages, the RMS of our cryogenic wind tunnel was comparable to that of ETW, which was advantageous for the wind tunnel with cross-sectional area eight times larger than ours. In the low-temperature range ( $< 200$  K), our cryogenic wind tunnel still met the requirements of China Military Standards in the subsonic stage. To be honest, the flow quality

decreased for Mach numbers greater than 1.0 with the limitation of the cross-sectional size and low-temperature effect. Its RMS deviation was still within 1.5 times of that for ETW. Especially, the RMS deviations of Mach number 1.3 at the core position was controlled within 0.011 in low and high temperatures, which validated the new concepts of our design.

## 5. Conclusions

The present study proposed a new design concept of a single-jack variable Mach number nozzle for a cryogenic transonic wind tunnel. The design and calibration were carried out in a 0.3-m cryogenic wind tunnel. The conclusions are as follows:

- An equal-thickness flexible plate could achieve a good agreement with the design contour, and deviations between the designed and measured contours at room temperature were within  $\pm 0.1$  mm.
- As the temperature decreased, the flow velocity slightly decreased in the test section, and the decreasing amplitude of the Mach number in the subsonic range was within 0.002, while it became 0.004-0.006 above Mach number 1.0.
- When the temperature declined, the RMS deviation increased. However, under subsonic conditions, the Mach number RMS deviation was not greater than 0.002, while the RMS deviation of Mach number 1.3 was controlled within 0.011 in low and high temperatures, which surpasses the other existing wind tunnels.

### Acknowledgements

The authors acknowledge financial support from National Natural Science Foundation of China (NSFC) (Grant No. 51935006).

## References

1. BISSHOPP K.E., DRUCKER D.C., 1945, Large deflection of cantilever beams, *Quarterly of Applied Mathematics*, **3**, 3, 272-275
2. CHEN P., WU F., XU, J., FENG X., YANG Q., 2016, Design and implementation of rigid-flexible coupling for a half-flexible single jack nozzle, *Chinese Journal of Aeronautics*, **29**, 6, 1477-1483
3. CRESCI R.J., 1958, *Tabulation of Coordinates for Hypersonic Axisymmetric Nozzles. Part 1: Analysis and Coordinates for Test Section Mach Numbers of 8, 12 and 20*, Polytechnic Institute of Brooklyn, Department of Aeronautical Engineering and Applied Mechanics
4. DAVIS R.L., NI R.H., CARTER J.E., 1987, Cascade viscous flow analysis using the Navier-Stokes equations, *Journal of Propulsion and Power*, **3**, 5, 406-414
5. GREEN J., QUEST J., 2011, A short history of the European Transonic Wind Tunnel ETW, *Progress in Aerospace Sciences*, **47**, 5, 319-368
6. GUO S.G., WANG Z.G., ZHAO Y.X., 2015, Design of a continuously variable Mach-number nozzle, *Journal of Central South University*, **22**, 2, 522-528
7. HARTZUIKER J., 1984, The European Transonic Wind-tunnel ETW: a cryogenic solution, *The Aeronautical Journal*, **88**, 879, 379-394
8. HARTZUIKER J., 1986, The European Transonic Windtunnel ETW-Design concepts and plans, *14th Aerodynamic Testing Conference*, **731**
9. HENSCH A.K., GUNTERMANN P., LONGO R., QUEST J., OKFEN P., RISIUS S., KLEIN C., ONDRUS V., BEIFUSS U., SCHABER S., 2019, Investigation of Hybrid Laminar Flow Control (HLFC) on a 2D-model in the cryogenic Pilot European Transonic Windtunnel (PETW), *AIAA Scitech 2019 Forum*, **1181**

10. HOWELL L.L., LEONARD J.N., 1997, Optimal loading conditions for non-linear deflections, *International Journal of Non-Linear Mechanics*, **32**, 3, 505-514
11. KITTEL P., 2012, *Advances in Cryogenic Engineering*, Springer Science & Business Media
12. LAI H., CHEN W.H., SUN D.W., NIE X.T., ZHU C.J., 2020, The structural design for 0.3m cryogenic continuous transonic wind tunnel (in Chinese), *Journal of Experiments in Fluid Mechanics*, **34**, 5, 89-96
13. LIAO D.X., HUANG Z.L., CHEN Z.H., 2014, Review on large-scale cryogenic wind tunnel and key technologies (in Chinese), *Journal of Experiments in Fluid Mechanic*, **28**, 2, 1-6+20
14. LV Z., XU J., WU F., CHEN P., WANG J., 2018, Design of a variable Mach number wind tunnel nozzle operated by a single jack, *Aerospace Science and Technology*, **77**, 299-305
15. NIU W.C., JU Y.L., 2021, System design and experimental verification of an internal insulation panel system for large-scale cryogenic wind tunnel, *Cryogenics*, **115**, 103279
16. REESE D., DANEHY P., JIANG N., FELVER J., RICHARDSON D., GORD J., 2019, Application of resonant femtosecond tagging velocimetry in the 0.3-meter transonic cryogenic tunnel, *AIAA Journal*, **57**, 9, 3851-3858
17. RIVERS M.B., LYNDE M.N., CAMPBELL R.L., VIKEN S.A., CHAN D.T., WATKINS A.N., GOODLIFF S.L., 2019, Experimental investigation of the NASA common research model with a natural laminar flow wing in the NASA Langley National Transonic Facility, *AIAA Scitech 2019 Forum*, **2189**
18. ROSEN J., 1955, The design and calibration of a variable Mach number nozzle, *Journal of the Aeronautical Sciences*, **22**, 7, 484-490
19. SIVELLS J.C., 1978, *A Computer Program for the Aerodynamic Design of Axisymmetric and Planar Nozzles for Supersonic and Hypersonic Wind Tunnels*, Arnold Engineering Development Center Arnold AFB TN
20. XU K., LIU H., XIAO J., 2021, Static deflection modeling of combined flexible beams using elliptic integral solution, *International Journal of Non-Linear Mechanics*, **129**, 103637
21. ZHANG A.M., CHEN G.M., 2013, A comprehensive elliptic integral solution to the large deflection problems of thin beams in compliant mechanisms, *Journal of Mechanisms and Robotics*, **5**, 2
22. ZHANG Z., NIU L., 2015, Current status and key technologies of cryogenic wind tunnel, *Cryogenics*, **2**, 57-62

*Manuscript received February 8, 2022; accepted for print September 16, 2022*